







Optical magnetic field enhancement using ultrafast azimuthally polarized laser beams and tailored metallic nanoantennas

RODRIGO MARTÍN-HERNÁNDEZ,^{1,2,†}  LORENZ GRÜNEWALD,^{3,4,†}  LUIS SÁNCHEZ-TEJERINA,^{1,5} 
LUIS PLAJA,^{1,2}  ENRIQUE CONEJERO JARQUE,^{1,2}  CARLOS HERNÁNDEZ-GARCÍA,^{1,2,6}  AND
SEBASTIAN MAI^{3,7} 

¹Grupo de Investigación en Aplicaciones del Láser y Fotónica, Departamento de Física Aplicada, Universidad de Salamanca, E-37008 Salamanca, Spain

²Unidad de Excelencia en Luz y Materia Estructuradas (LUMES), Universidad de Salamanca, E-37008 Salamanca, Spain

³Institute of Theoretical Chemistry, Faculty of Chemistry, University of Vienna, 1090 Vienna, Austria

⁴Vienna Doctoral School in Chemistry (DoSChem), Faculty of Chemistry, University of Vienna, 1090 Vienna, Austria

⁵Departamento de Electricidad y Electrónica, Universidad de Valladolid, 47011 Valladolid, Spain

⁶e-mail: carloshergar@usal.es

⁷e-mail: sebastian.mai@univie.ac.at

[†]These authors contributed equally to this work.

Received 13 November 2023; revised 1 February 2024; accepted 14 February 2024; posted 15 February 2024 (Doc. ID 511916); published 1 May 2024

Structured light provides unique opportunities to spatially tailor the electromagnetic field of laser beams. These include the possibility of a sub-wavelength spatial separation of their electric and magnetic fields, which would allow isolating interactions of matter with pure magnetic (or electric) fields. This could be particularly interesting in molecular spectroscopy, as excitations due to electric and—usually very weak—magnetic transition dipole moments can be disentangled. In this work, we show that the use of tailored metallic nanoantennas drastically enhances the strength of the longitudinal magnetic field carried by an ultrafast azimuthally polarized beam (by a factor of ~ 65), which is spatially separated from the electric field by the beam's symmetry. Such enhancement is due to favorable phase-matching of the magnetic field induced by the electric current loops created in the antennas. Our particle-in-cell simulation results demonstrate that the interactions of moderately intense ($\sim 10^{11}$ W/cm²) and ultrafast azimuthally polarized laser beams with conical, parabolic, Gaussian, or logarithmic metallic nanoantennas provide spatially isolated magnetic field pulses of several tens of Tesla.

Published by Chinese Laser Press under the terms of the [Creative Commons Attribution 4.0 License](https://creativecommons.org/licenses/by/4.0/). Further distribution of this work must maintain attribution to the author(s) and the published article's title, journal citation, and DOI.

<https://doi.org/10.1364/PRJ.511916>

1. INTRODUCTION

Current optical techniques allow us to tailor laser light in all spatiotemporal dimensions, opening the possibility to structure the electromagnetic field in unprecedented ways [1,2]. One of the most intriguing developments, as highlighted in Ref. [3], lies in the ability to separate the electric field (E-field) and the magnetic field (B-field) of a laser beam. This presents an opportunity to disentangle interactions between purely electric and purely magnetic field-matter interactions. There are several approaches to isolate (i.e., to spatially separate) the E-field and the B-field components of an optical laser beam. For example, close to mirror surfaces, interference effects lead to different wavelength-dependent positions of the nodes of the E-field and B-field, which could affect the emission rate of

electric and magnetic dipole transitions of molecules close to the surface [4–6]. Similar effects are observed near dielectric or metal photonic nano-structures [7–9], in cavities (referred to as Purcell effect) [10], or in metasurfaces [11,12], where the manipulation of electric and magnetic dipole emissions has been one focus application. A potentially simpler approach consists of using two counter-propagating beams, where the E-field and B-field nodes can be separated spatially; such a scheme has been proposed, e.g., utilizing high-power laser beams for applications in attoscience [13].

Alternatively, spatially isolated E-fields and B-fields can be achieved with structured light techniques [1], which allow precisely sculpting the spatial distribution of amplitude, phase, and polarization state of a laser beam. One prominent example of

such structured light beams is vector beams, i.e., laser beams with spatially dependent polarization states [14]. The most common vector beams are radially polarized and azimuthally polarized beams (APBs), which show a cylindrically symmetric linearly polarized pattern [15]. They are of fundamental interest in applications such as optical communication technology, nano-lithography, and quantum key distribution [3,16,17]. In an APB, the B-field is radially polarized, whereas the E-field is azimuthally (i.e., tangentially to the beam circumference) polarized. This polarization state acts similarly to an oscillating closed current loop, thus inducing a longitudinally polarized B-field along the beam's propagation axis upon focusing of the APB. Given that the E-field vanishes on the propagation axis due to symmetry constraints (i.e., it shows a singularity), in an APB the longitudinal B-field is locally isolated from the E-field [see Fig. 1(a)]. One major advantage of this scheme is that the position of the isolated B-field does not move when changing the wavelength, unlike related setups that exploit interference close to mirror surfaces [4–6]. Such isolated B-fields have been proposed as a tool for several applications, e.g., magnetic spectroscopy [18–20] or force microscopy [21,22] employing sub-tesla B-fields, or ultrafast nonlinear magnetization [23] employing multi-tesla B-fields.

The possibility to isolate intense B-fields provides interesting opportunities in optical spectroscopy. A considerable fraction of our knowledge related to electronic states of atoms and molecules has been obtained by spectroscopic investigations at optical wavelengths, e.g., by UV/Vis absorption spectroscopy. At optical wavelengths, the interaction between the E-field component of the absorbed light and the molecular transition electric dipole (ED) moment dominates [24–27], whereas the interaction of the B-field component of light with the molecular transition magnetic dipole (MD) moment is orders of magnitude weaker [28]. Although weak, MD transitions are potentially of strong interest in the elucidation of “dark” states, which cannot easily be accessed or observed via strong ED

transitions (e.g., parity-conserving transitions in metal atoms or $n\pi^*$ states) [5,29–34]. In such systems, the direct observation of MD transitions would enable a more detailed investigation of the electronic/vibronic structure of the target molecules, as well as investigations of photoinduced processes initiated in such states. In order to observe MD transitions, which are typically concealed by the much stronger ED transitions, special strategies are required. Circular dichroism (CD) or magnetic circular dichroism (MCD) are both sensitive to MD transitions but are only applicable to certain kinds of molecular systems (chiral molecules or ones that exhibit certain near-degeneracies, respectively) [35]. Hence, it would be desirable to have a general approach that does not only work in certain systems (e.g., those with very large MD moments or forbidden ED transitions). As discussed previously in the literature, such a general approach would require that the E-field is strongly suppressed at the target molecule's position [27]. Additionally, due to the intrinsic weakness of MD transitions, it would be advantageous to employ a B-field that is as strong as possible. The combination of such spatially isolated and intense oscillating B-fields could then form the basis for a general “MD-only optical spectroscopy.”

APBs are excellent candidates for this purpose, as recently demonstrated by Kasperczyk *et al.* [27], who employed a focused APB to record a luminescence excitation spectrum of Eu^{3+} -doped Y_2O_3 nanoparticles. In particular, at the center of the beam, emission was only detected when the wavelength was tuned to the relevant MD transition of Eu^{3+} , whereas no emission was observed when exciting the ED transition. This shows that suppression of the E-field can be used to observe MD-exclusive transitions. However, as MD transitions are intrinsically weak, a further enhancement of the B-field strength, beyond what is achievable by a focused APB, would be desirable. A simultaneous isolation and enhancement of the B-field would not only enable MD-only spectroscopy but also provide opportunities for other applications, e.g., in laser-driven

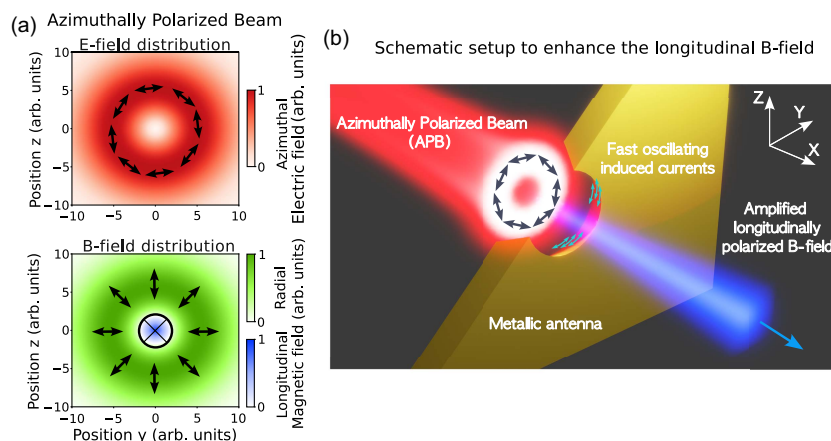


Fig. 1. (a) Azimuthally polarized beam (APB) electric field (E-field, upper panel) and magnetic field (B-field, lower panel) spatial distributions. The arrows in each panel indicate the polarization direction. The donut-shaped radial B-field polarization distribution is depicted in green, while the blue corresponds to the on-axis longitudinal component (out of plane). (b) The APB (red beam) interacts with a metallic nanoantenna, inducing strong and fast oscillating currents in the inner surface of the antenna (light blue, double headed arrows). As a result of the coherent superposition of the B-fields created by the ultrafast induced currents, the longitudinally polarized magnetic field (blue beam) of the APB is amplified by more than one order of magnitude.

particle acceleration [36–38], photoinduced force microscopy [22,39], or other nanoscale force microscopy techniques [40,41].

The generation of APBs in the visible and near-infrared can be achieved with the use of spatial light modulators [42], uniaxial or biaxial crystals [43,44], optical fibers [45], or nanostructured half-waveplates (known as s-waveplates) [46], which modify the polarization state distribution of the incident light beam accordingly. A very attractive possibility to generate intense APBs—and thus intense and isolated B-fields—is to move to the ultrafast regime. Recent experiments have shown the possibility of generating vector beams in the near-infrared/femtosecond scale using s-waveplates [47], or even in the extreme ultraviolet/attosecond regime through high harmonic generation [48]. But, most notably, the combination of ultrafast vector beams and nanoantennas, where the longitudinal B-field is enhanced through the creation of oscillating current loops, has pioneered the generation of isolated tesla-scale magnetic fields [49,50], ideal candidates for ultrafast MD-only spectroscopy and other applications. This combination is one of a few ways to achieve simultaneous isolation and enhancement of B-fields, unlike several other schemes focusing on isolation [4–6] or enhancement [51–53].

In this work, we explore the use of specifically tailored nanoantennas—rotationally symmetric, metallic nano-structures [see Fig. 1(b)]—to enhance the spatially isolated longitudinal B-field of an ultrafast APB. We perform particle-in-cell (PIC) simulations, using the OSIRIS code [54–56], to simulate and analyze the spatiotemporal evolution of an ultrafast APB interacting with metallic nanoantennas of cylindrical [49] and various other shapes. To understand the underlying physics, we develop an analytical model based on the retarded potential formalism [57,58], which allows us to explain the enhancement mechanism in terms of favorable phase-matching between ultrafast electric currents. Expanding upon the previous simulations [49], we investigate the capabilities of sloped and curved antennas—conical, parabolic, Gaussian, and logarithmic—with varying geometric parameters for B-field enhancement and simultaneous E-field suppression of incident APBs. We also show how the enhanced B-field spatial distribution depends on the antenna shape. Our work provides a rigorous study of how to enhance and tailor the spatial distribution of the B-field carried by an ultrafast APB through the use of custom metal nanoantennas in the optical, femtosecond regime.

2. METHODS

In our simulations, we predict the temporal and three-dimensional spatial evolution of ultrafast APBs with the goal of enhancing and isolating its longitudinal B-field. To do so, we explore its interaction with metallic antennas with different shapes and geometry parameters.

A. Characterization of an Ultrafast Azimuthally Polarized Laser Beam

Throughout our simulations, we employ an APB as our incident laser beam. In principle, it is possible to formulate cylindrical vector beams (like APBs) in the Bessel–Gauss framework [15], which provides exact solutions of the full Helmholtz

equation. Instead, we formulate our incident beam at the entrance plane of the simulation box in the paraxial approximation, propagating in a vacuum along the x direction. In cylindrical coordinates $\vec{r} = (\rho, \phi, x)^T$, with the focus placed at the origin ($x = 0$), the electromagnetic field of such an APB can be written as

$$\vec{E}(\vec{r}, t) = E_0 f(t) e^{i\frac{2\pi}{\lambda}(x-ct)} \frac{\sqrt{2}}{w_0} \rho e^{-\frac{\rho^2}{w_0^2}} \vec{u}_\phi, \quad (1)$$

$$\vec{B}(\vec{r}, t) = -\frac{E_0}{c} f(t) e^{i\frac{2\pi}{\lambda}(x-ct)} \frac{\sqrt{2}}{w_0} e^{-\frac{\rho^2}{w_0^2}} \left(\rho \vec{u}_\rho + \frac{\lambda}{\pi} \left(1 - \frac{\rho^2}{w_0^2} \right) e^{i\frac{\pi}{2}} \vec{u}_x \right), \quad (2)$$

where w_0 is the beam waist, λ is the central wavelength, and c is the vacuum speed of light. \vec{u}_ρ , \vec{u}_ϕ , \vec{u}_x are unit polarization vectors, and $f(t) = \sin^2(\pi \frac{t}{\tau_{\text{end}}})$ is the temporal envelope function for $0 \leq t \leq \tau_{\text{end}}$. To alleviate the high computational cost of simulations, we employed a short laser pulse with a pulse duration $\tau_{\text{end}} = 10$ fs.

The spatial distributions of the E-field and B-field intensities at the focal plane are represented in Fig. 1(a). In contrast to a fundamental Gaussian beam, the E-field peak amplitude $E_{\text{max}} = E_0/\sqrt{e}$ is not reached at the minimum waist w_0 but instead at $\rho_{\text{max}} = w_0/\sqrt{2}$. Also note that the radially polarized (\vec{u}_ρ) component of the B-field spatially coincides with the azimuthally polarized (\vec{u}_ϕ) E-field. Directly on-axis ($\rho = 0$), all transverse (\vec{u}_ρ and \vec{u}_ϕ) E-field and B-field components vanish, and only the longitudinally polarized B-field (\vec{u}_x) remains non-zero, reproducing the above-mentioned E-field–B-field separation. The latter component increases with decreasing waist parameter w_0 , i.e., upon focusing [18].

Within our PIC simulations (see details below), we set the minimum waist to $w_0 = 2.5$ μm and the E-field peak amplitude to $E_{\text{max}} = 1.2$ GV/m (equivalent to $E_0 = 1.98$ GV/m and a peak intensity of 1.9×10^{11} W/cm² at ρ_{max}). With the above parameters, the longitudinal B-field peak amplitude at the focus of the beam is $B_{\text{max}}(\rho = 0, x = 0) = 0.6$ T. The central wavelength is set to $\lambda = 527.5$ nm, motivated by the excitation wavelength of the prominent ${}^7F_0 \rightarrow {}^5D_1$ MD-exclusive absorption band in the Eu³⁺ ion [59,60], which has been previously used to demonstrate exclusive MD excitation via an APB [27].

B. Simulation Framework

We propagate the described APB numerically using the Maxwell solver implemented in the PIC package OSIRIS [54–56]. Here, the E-fields and B-fields are represented on a 3D mesh. In our simulations, we construct the incident APB as the superposition of two Hermite–Gauss beams that are orthogonally polarized [15]. In our simulations, we describe the metallic antenna material as spatially restricted neutral plasma, which within PIC is described by charged macroparticles that move according to Newton's equation and are self-consistently coupled to the E-field and B-field propagation [61–63].

OSIRIS internally works with a suitably normalized system of dimensionless units, which can be scaled as desired *a posteriori*. In order to relate our simulations to the parameters mentioned above (minimum waist, peak amplitude, central

wavelength), we chose a reference frequency with a value of $\omega_R = 2\pi c/527.5$ nm.

The neutral plasma representing the antenna material is made up of two particle species, motivated by the presence of electrons and gold ions in metallic gold. For both species, we consider a particle species density $n_e = n_n = 5.9 \times 10^{22}$ cm⁻³ (assuming monovalent gold ions). The mass-to-charge ratio for the gold ions was set to $m_{\text{Au}}/q_{\text{Au}} = 361630m_e/e$. Note that such a neutral plasma cannot accurately represent material parameters such as the frequency-dependent electric permittivity or magnetic permeability. Hence, we do not include a dielectric substrate in our simulations, as is commonly used to support thin metal films [64]. Given that our total pulse duration (10 fs) is below the room temperature carrier relaxation time of the metallic antenna (27.3 fs in Au, ~ 36 fs in other metals as Ag or Cu [65]), the material properties can be approximated with a free electron model, described by this neutral plasma. We also note that the fluence of such short pulses (1.9×10^{11} W/cm² times 10 fs yields 1.9 mJ/cm²) is significantly lower than the laser-induced damage threshold of Au (about 0.2 J/cm² at about 800 nm for films of at least 0.2 μm thickness) [66] and other metals. For larger pulse durations, relaxation and damping effects should be taken into account for a realistic description, as they would lower the ring currents [67] and thus strongly affect the achievable B-field enhancement. However, the cylindrical symmetry of the setup would maintain the E-field–B-field isolation even when considering relaxation and damping effects.

C. Antenna Shapes and Geometry Parameters

In this work we explore the B-field enhancement and isolation in five different antennas: cylindrical, conical, parabolic, Gaussian, and logarithmic. The investigated shapes all exhibit cylindrical symmetry around the optical axis of the laser beam.

Note that deviations from this symmetry (i.e., using an elliptical aperture) were shown to diminish the B-field enhancement [49]. The profiles for the proposed antennas are shown in Figs. 2(a)–2(e), and the corresponding parameters are detailed in Table 1 in Appendix A.

In our simulations for conical, cylindrical, and logarithmic antennas we use a box size of $l_x = 2.5$ μm (longitudinal) and $l_y = l_z = 13$ μm (transverse). With the employed omnidirectional spatial resolution of 9.0 nm, this yields a grid of $279 \times 1445 \times 1445$ cells. For the parabolic and Gaussian shapes, the longitudinal box size was doubled to $l_x = 5.0$ μm (with $558 \times 1445 \times 1445$ cells). This was necessary to retain the B-field maximum inside the simulation box for the wide set of geometry parameters that we consider. All antennas are centered in the longitudinal direction at the beam focus, which is placed at $x_0 = l_x/2$. The simulation time was set to 15 fs for the conical, cylindrical, and logarithmic antennas, and to 30 fs for the parabolic and Gaussian ones, with a temporal resolution of 5.6 as, which is well within the limits given by the Courant-Friedrichs-Lewy (CFL) condition [68]. For all walls of the simulation box, we employ perfectly matched layers with 90 nm thickness as absorbing boundary conditions [69].

The OSIRIS input files and evaluation scripts are made publicly available at Zenodo [70].

3. RESULTS AND DISCUSSION

In this section, we start with an analysis of the B-field enhancement upon the optimization of the antenna geometries with a linear orifice slope along the optical axis, i.e., cylindrical and conical antennas. Thereafter, we introduce an analytical model that allows us to understand the physics beyond the longitudinal B-field enhancement in a cylindrical antenna. Then, we extend our study to antenna geometries that present a

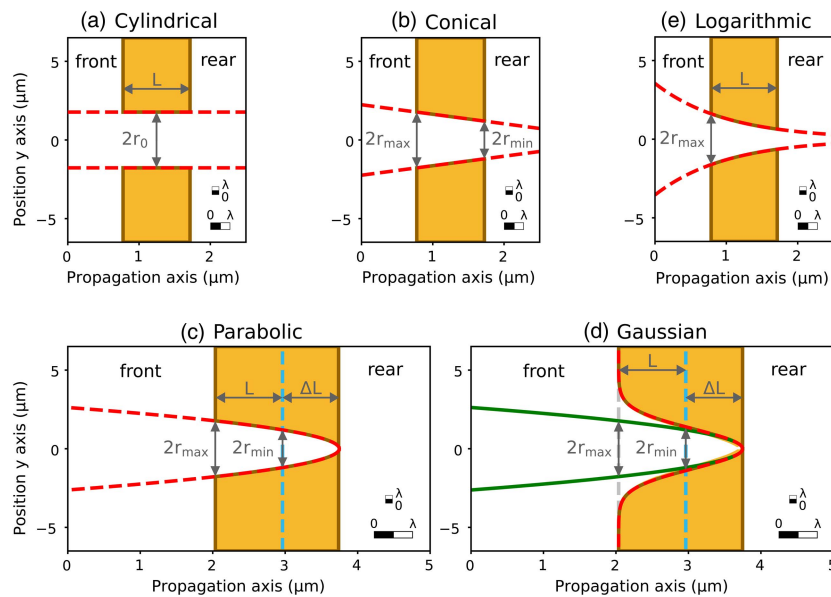


Fig. 2. Vertical section of the considered antenna shapes (all antennas are cylindrically symmetric around the propagation axis). The orifice dimensions are governed by analytical functions (see Table 1, indicated by the red dashed lines). The Gaussian antenna case is parametrized to fit to the parabola shape (green). The shapes are labeled (a)–(e) in the order they are discussed below. The scale bars show the employed wavelength (527.5 nm) relative to the transverse and longitudinal dimensions of the antennas.

non-linear profile along the optical axis, i.e., parabolic, Gaussian, and logarithmic antennas. Finally, we analyze the contrast between B-fields and E-fields intensities for all proposed antenna geometries to quantify the spatial isolation of the intense longitudinal B-fields.

A. Magnetic Field Enhancement for Linearly Sloped Antennas

The antennas with the simplest shapes are the cylindrical and the conical antennas. Here, we present PIC numerical simulations that show the B-field enhancement in these cases.

1. Cylindrical Antenna

In a previous study by Blanco *et al.* [49], cylindrical metallic antennas were proposed for enhancing the B-field of an APB. The study investigated in detail the influence of the antenna radius r_0 on the B-field enhancement. It was found that the highest B-field is obtained when $r_0 = \rho_{\max}$, i.e., when the antenna radius coincides with the radial position where the E-field of an APB reaches its maximum amplitude [see Eq. (1)]. We note that this condition implies that the diameter (and thus the inner circumference) of the antennas is several times the wavelength of the employed fields (see Fig. 2). Thus, plasmonic resonances (i.e., localized surface plasmons) do not contribute to the induced currents in the antennas [71,72].

Here, we expand upon these investigations exploring the role of the antenna thickness L (considering $r_0 = \rho_{\max}$). As presented in Fig. 3(a), the maximum B-field strength grows from 4.5 T for the thinnest antenna, with $L = 0.03 \mu\text{m}$, to

7.5 T that is reached at $L = 0.3 \mu\text{m}$. For larger L , the maximum B-field strength oscillates roughly between 6.5 and 7.5 T. Our simulations then show that once a minimum thickness of $L = 0.3 \mu\text{m}$ is achieved, thicker antennas do not provide higher longitudinal B-fields but also do not diminish the B-field strength; thus, the thickness can be adapted to practical needs, e.g., thermal robustness.

In Fig. 3(b), we analyze the B-field strength along the propagation axis (x) for different values of the antenna thickness L . It can be seen that similar maximum B-fields are obtained over a wide range of positions before, within, and behind the antenna (depicted by the gray dashed lines). The needle-shaped B-field distribution for a particular case ($L = 0.3 \mu\text{m}$) is represented in Fig. 3(c). Unlike the large spatial extent of the B-field needle along the propagation axis, the B-field strength drops quickly (over tens of nanometers) when moving away from the optical axis in the transverse direction. Consequently, experiments relying on the isolated and enhanced B-field in a cylindrical antenna would require precise placement of the target particles/molecules. Figure 3(c) also shows that the magnetic needle is surrounded by several concentric rings with half-wavelength width. The rings have alternating polarization directions, which might be relevant for the interaction with magnetic materials.

2. Conical Antenna

The saturation observed in Fig. 3(a) motivated us to modify the geometry to a conically shaped antenna, in order to maximize the direct interaction between the APB and the metal. The conical antenna geometry is a generalization of the cylindrical

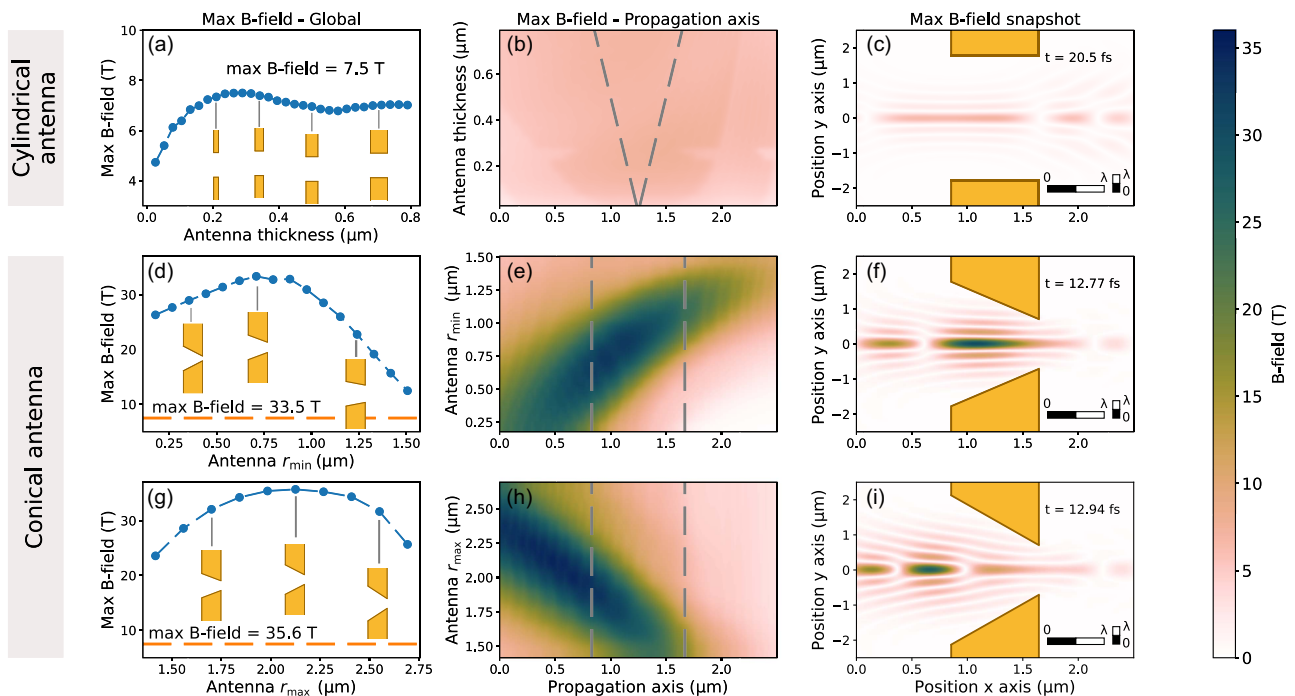


Fig. 3. Maximum achievable longitudinal B-field strength (a)–(c) for different antenna thicknesses of the cylindrical antenna, (d)–(f) for the r_{\min} scan, and (g)–(i) for the r_{\max} scan of the conical antenna. (a), (d), (g) In the first column, the maximum longitudinal B-field on the propagation axis is shown along the scanned parameter, together with the B-field of the optimized cylindrical antenna (orange dashed line). (b), (e), (h) The second column reveals the distribution of the B-field strength along the propagation axis, the longitudinal extent of the aperture (gray dashed lines). (c), (f), (i) In the third column, a temporal snapshot of the longitudinally polarized B-field, when the maximum amplitude is reached, is presented for the different scans.

antenna that exhibits a linear slope. We assume an open conical antenna facing the incident beam, i.e., with front radius r_{\max} and rear radius r_{\min} such that $r_{\max} > r_{\min} > 0$. The antenna thickness L is fixed at $L = 0.8 \mu\text{m}$, the largest value we investigated for the cylindrical antenna.

In order to find values of r_{\max} and r_{\min} that optimize the B-field strength, in Fig. 3(d) we first scan r_{\min} while keeping r_{\max} fixed at the optimal radius for cylindrical aperture ($r_0 = 1.77 \mu\text{m}$). Note that the far right of the figure ($r_{\min} = r_0 = 1.77 \mu\text{m}$) corresponds to the cylindrical case. If r_{\min} is then reduced, we can observe a significant increase in the maximum B-field strength, reaching a peak value of 33.5 T for $r_{\min} \sim 0.75 \mu\text{m}$. This translates into a gain factor of ~ 50 compared to the freely propagating focused APB without any antenna, and a gain factor of ~ 5 compared to the optimized cylindrical antenna (orange line). In this case, the B-field is longitudinally focused in a relatively narrow region, as exhibited in the spatial distributions shown in Figs. 3(e) and 3(f), as long as r_{\min} is clearly smaller than r_{\max} . The maximum B-field is found in the rear of the antenna position for large r_{\min} (i.e., for nearly cylindrical antennas) and moves in front of the antenna for decreasing r_{\min} (i.e., for more strongly sloped walls), as depicted in Fig. 3(e). The highest achieved B-field strengths are obtained when the B-field peak is located inside the antenna ($0.85 \mu\text{m} < x < 1.65 \mu\text{m}$). This shows that by varying r_{\min} —or analogously, the slope of the antenna walls—we can tune both the gain factor and the B-field peak position (i.e., we can switch from a reflective to a transmissive antenna), which is potentially of high interest for the envisioned applications. Here, a dielectric substrate in the rear of the antenna might affect the B-field peak position for transmissive antennas, although E-field–B-field isolation should not be compromised.

In order to fully optimize the B-field enhancement in the interaction of an APB with conical antenna, we show in Fig. 3(g) a scan over the front radius (r_{\max}) for a fixed rear radius of $r_{\min} = 0.75 \mu\text{m}$. The optimal value is obtained for $r_{\max} = 2.13 \mu\text{m}$, which is higher than r_0 , and further increases the B-field strength to 35.6 T (which conveys a gain factor of ~ 55 compared to the free beam simulation). Figure 3(h) shows the position along the propagation axis of the maximum B-field depending on r_{\max} . We note that larger r_{\max} (more steeply sloped walls) moves the B-field peak position towards the front part of the antenna. The spatial snapshot presented in Fig. 3(i), shows that the optimal set of parameters ($L = 0.8 \mu\text{m}$, $r_{\min} = 0.75 \mu\text{m}$, $r_{\max} = 2.13 \mu\text{m}$) leads to a localized B-field peak, located slightly before the antenna.

B. Analytical Model

To gain a better understanding of the physics underlying the interaction of an APB and a general conical antenna, we develop an analytical model based on the retarded potential formalism [57,58] (see complete derivation in Appendix B). The total longitudinal B-field (B_x) generated by a thick antenna is modelled as the coherent superposition of the fields (B_{loop}) generated by several, infinitesimally thin current loops induced in the metallic antenna inner surface. As the total B-field (B_x) arises from this superposition, the phase difference between each B_{loop} plays a major role in the final B-field enhancement. This is in analogous to the phase matching effect in nonlinear

optics [73]. Thus, in this model the total longitudinal B-field, B_x , can be expressed in cylindrical coordinates by the following integral:

$$\begin{aligned} B_x(x, t) &= \int dx' |B_{\text{loop}}(x, x')| e^{i(\phi(x, x') - \frac{2\pi ct}{\lambda})} \\ &= 2\pi \int dx' j_0(x') \frac{\rho(x')^2}{c \rho(x')^2 + (x - x')^2} \\ &\quad \times \left(\left(\frac{2\pi}{\lambda} \right)^2 + \frac{1}{\rho(x')^2 + (x - x')^2} \right)^{1/2} \\ &\quad \times e^{i\frac{2\pi}{\lambda}(x' + \sqrt{\rho(x')^2 + (x - x')^2} - ct) - i \arctan(\frac{2\pi}{\lambda} \sqrt{\rho(x')^2 + (x - x')^2})}, \quad (3) \end{aligned}$$

where $j_0(x')$ is the current density distribution, and $\rho(x')$ is the aperture radius at x' . The variable x' is the longitudinal position of the infinitesimally thin current loops, over which integration is carried out, along the propagation axis.

The spatial phase term $\phi(x, x')$ in Eq. (3) can be divided in two terms, $\phi(x, x') = \phi_1(x, x') + \phi_2(x, x')$. The first phase term $\phi_1(x, x') = \frac{2\pi}{\lambda}(x' + \sqrt{\rho(x')^2 + (x - x')^2})$ represents a fast spatial oscillation experienced by the B-field when propagating from the source point in the current loop to the observation point on the optical axis. The second term, $\phi_2(x, x') = -\arctan(\frac{2\pi}{\lambda} \sqrt{\rho(x')^2 + (x - x')^2})$, is a Gouy phase-like term, being minimal at the current loop center ($x = x'$) and increasing up to $\frac{\pi}{2}$ for $|x - x'| \gg 0$, i.e., far from the current loop origin. The main contribution to the phase-matching-like process is given by the first phase term ϕ_1 , as ϕ_2 remains almost constant in our region of interest.

The proposed analytical model is compared with the simulation results for the conical antenna in Fig. 4. Figures 4(a) and 4(b) show the comparison of the maximum B-field strength of the previous two scans already presented in Figs. 3(d) and 3(g), whereas Figs. 3(c) and 3(d) show the spatial extent of the maximum analytical B-field strength, analogous to Figs. 3(e) and 3(h).

The excellent agreement between the analytical model and the numerical simulations allows us to identify the physics underlying the B-field enhancement mechanism. According to Eq. (3), the longitudinal B-field strength on axis is affected by the antenna shape in two ways: through the current density distribution $j_0(x')$ and through the accumulated phase ϕ . On the one hand, the current density distribution is given by $j_0(x') = q^2 n \frac{E_0(x')}{\sqrt{2m_e \omega}} (1 - \cos(\arctan(\frac{\partial \rho(x')}{\partial x'})))$, as detailed in Appendix B. The dependence on the slope of the antenna walls ($\frac{\partial \rho(x')}{\partial x'}$) is such that the current density is largest if the incident beam is perpendicular to the wall, which increases the B-field strength in steeply sloped conical antennas. On the other hand, the B-field strength is controlled by the constructive interference given by $\phi(x, x')$. Taking into account the prominent role of ϕ_1 , optimal constructive interference would require a parabolic antenna shape, which shows that, in general, a curved antenna optimizes the maximum B-field strength.

Thus, thanks to our analytical model we can conclude that the mechanism of B-field enhancement in the conical antenna is mostly based on the constructive interference of the local B-fields created by the transverse current loops distributed along the propagation axis. Depending on the slope of the antenna, this

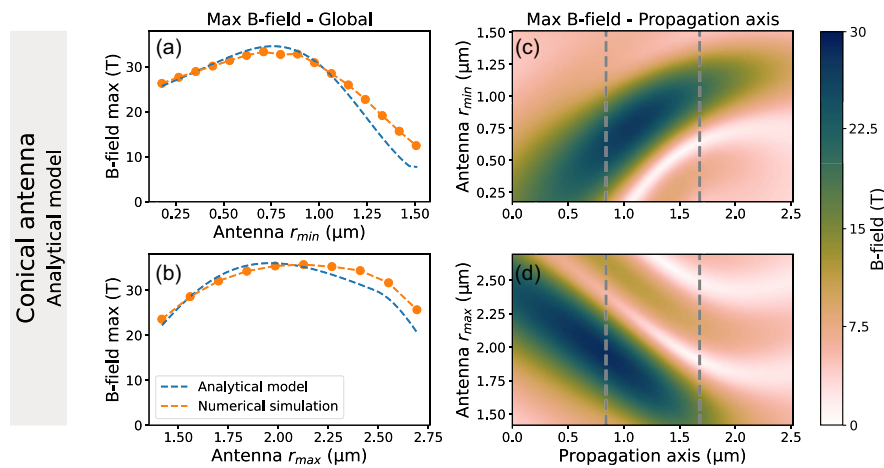


Fig. 4. (a), (b) Total B-field strength for cone orifice radius scans of the rear side [r_{\min} (a)] and the front side [r_{\max} (b)]. The dotted orange line denotes the results retrieved from numerical PIC simulations, whereas the blue dashed line illustrates the predicted B-field strength based on the derived analytical model [see Eq. (3)]. (c), (d) Distribution of the analytically predicted B-field strength along the optical axis for cone orifice radius scans of the rear side [r_{\min} (c)] and the front side [r_{\max} (d)].

effect may confine the longitudinal B-field toward the front or the rear side of the antenna [see Figs. 4(b) and 4(d)].

C. Magnetic Field Enhancement for Curved Antennas

As motivated in the previous section, further B-field enhancement can be achieved by introducing curved antenna shapes that optimize the constructive interference of the B-field along the propagation axis. An additional advantage of curved/smooth antenna profiles is that they are possibly easier to manufacture [74–76] than antennas with perfectly straight walls. Thus, in this section, we investigate the interaction of an APB with parabolic, Gaussian, and logarithmic antennas, with the ultimate goal of controlling the enhancement of the longitudinal B-field, and its confinement along the propagation axis.

1. Parabolic Antenna

Parabolic reflectors or mirrors are broadly used in different technological applications such as acoustics, optics, or telecommunications to confine incoming electromagnetic waves at one spatial point, the focus [77]. While such antennas usually have macroscopic dimensions, there has been growing interest in using nano-sized parabolas as small-scale optical antennas [75,77,78]. Within the discussion of the analytical model for the conical antenna in Section 3.B, we showed that (near-)optimal constructive interference could be reached with a parabolic shape at its focal point.

The shape of a (truncated) parabolic antenna can be described with three independent parameters [see Fig. 2(c), Table 1]. First, the thickness L represents the distance between the front and rear sides of the antenna (analogous to the previous antennas). We fix the front-side parabola radius, r_{\max} , which is located at $x_0 - L/2$, to be at $r_{\max} = w_0\sqrt{2} = 1.77 \mu\text{m}$, as in the previous scans. The second independent parameter is the rear-side radius, r_{\min} , that we locate at $x_0 + L/2$. Then, L and r_{\min} fix the focal length of the antenna,

$f = \frac{r_{\max}^2 - r_{\min}^2}{4L}$, which shows that r_{\min} controls the curvature of the antenna. In order to investigate the B-field enhancement if the rear side of the antenna is closed, we introduce a third parameter, the cap thickness ΔL , which shifts the rear wall of the antenna to $x_0 + L/2 + \Delta L$, while keeping its focal length and focus position fixed.

The numerical simulation results that cover scans over the three parameters considered in a parabolic antenna are presented in Fig. 5. First, Figs. 5(a)–5(c) show the scan of r_{\min} over the range $0.89 \mu\text{m}$ to $\leq 1.94 \mu\text{m}$ (i.e., from $0.5r_{\max}$ to $1.1r_{\max}$). A maximum on-axis B-field strength of 18.5 T is reached for $r_{\min} \approx 1.17 \mu\text{m}$, which is about half the minimal waist. The scan shows a rather broad peak, with 90% of the maximum B-field strength reached between $1.0 \mu\text{m}$ and $1.4 \mu\text{m}$. While for small r_{\min} , the parabola is opening towards the front, for $r_{\min} = r_{\max}$ the antenna becomes cylindrical, and for $r_{\min} > r_{\max}$ opens towards the rear. This increase of r_{\min} is accompanied by a substantial B-field strength weakening, where a rear-opened parabola enhances the B-field even less than a cylindrical antenna. Moreover, the position of the maximum B-field shifts from the front side to the rear side along the scan, roughly following the focal point position, as shown in Fig. 5(b) (red line). Figure 5(c) shows the B-field distribution for the optimal r_{\min} parameter, showing a sub-wavelength spot of maximum B-field at about $x = 1.8 \mu\text{m}$, in front of the antenna.

Figures 5(d)–5(f) present the scan of the antenna thickness ($0.04 \mu\text{m} \leq L \leq 0.97 \mu\text{m}$), fixing the optimal values $r_{\max} = 1.77 \mu\text{m}$ and $r_{\min} = 1.17 \mu\text{m}$ from the previous scan. For small L , the maximum B-field strength increases approximately linearly. A maximum B-field of 25.4 T is reached at $L = 0.7 \mu\text{m}$, and a slow decrease of maximum B-field is observed beyond that point. For the optimal parameters (r_{\min} , r_{\max} , L), the maximum B-field spot is located within the antenna, as shown in Fig. 5(e). However, the maximum B-field spot can be shifted to the front or rear to some extent without compromising a strong B-field enhancement by varying L .

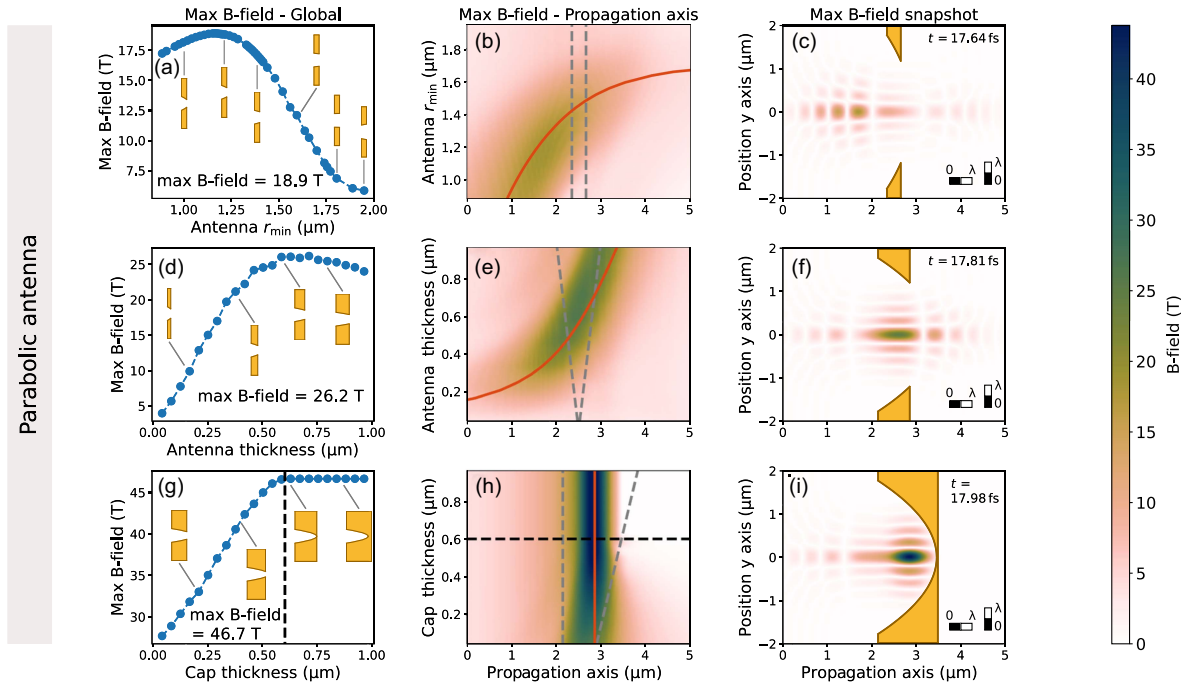


Fig. 5. Absolute B-field strength for the parabolic antenna for (a)–(c) scans of r_{\min} , (d)–(f) antenna thickness L , and (g)–(i) cap thickness ΔL . (a), (d), (g) In the first column, the maximum B-field on the propagation axis is shown depending on the scanned parameter. (b), (e), (h) The second column shows the distribution of the B-field strength along the propagation axis, the longitudinal extent of the aperture (gray dashed lines), and the position of the focal point (red, solid line). (c), (f), (i) In the third column, a temporal snapshot of the highest B-field strength is presented for the different scans. The dashed black line in (g) and (h) indicates when the antenna is closed.

The respective needle-like B-field distribution for the optimal antenna thickness is illustrated in Fig. 5(f).

Finally, in Fig. 5(g), we scan the cap thickness, ΔL , to investigate the B-field enhancement for closed parabolic antennas. The leftmost point is identical to the maximum in Fig. 5(d), and we scan over the range $0.0 \mu\text{m} \leq \Delta L \leq 1.0 \mu\text{m}$. Considering that the APB does not exhibit strong E-fields close to the beam axis, one would not expect significant additional ring currents and thus no strong B-field enhancement when closing the antenna. However, the scan in Fig. 5(g) evidences a strong, linear increase in B-field from 25 T to ~ 47 T. Once the antenna is fully closed (at $\Delta L = 0.6 \mu\text{m}$), no further increase in B-field strength is observed. This increase in maximum B-field strength is accompanied by a strong confinement of the B-field, as seen in Fig. 5(h). The same panel also shows that the B-field is zero behind the closed antenna, as expected. The strong confinement is also visible in Fig. 5(i), demonstrating that the magnetic needle is compressed to a spot by the parabolic aperture.

Overall, we demonstrate that the closed parabolic antenna shape can yield B-field strengths well above those achieved with the cylindrical and conical antenna shapes, though the B-field is localized inside the antenna. We revealed that—even in the near- or subwavelength regime where geometrical optics breaks down—the maximum B-field spot roughly coincides with the focal point of the parabolic reflector. Both properties can be of fundamental interest if B-fields should be tightly confined at predefined positions in an experimental setup.

2. Gaussian Antenna

Although a parabolic antenna shape can yield a large B-field enhancement, the precise fabrication of its nano-sized structure is challenging [77]. Therefore, next we investigate Gaussian-shaped antennas, where the curved slope approximates a parabolic curve to second order near the beam axis. Noticeably, nano-sized Gaussian-shaped holes in metal surfaces can be manufactured experimentally, e.g., via focused ion beam etching [79,80].

Our choice for the parameter scans in the (truncated) Gaussian antenna follows closely the ones for the parabolic antenna [see Figs. 2(c) and 2(d) for comparison]. We performed three scans, for the rear radius r_{\min} at $x_0 + L/2$, the antenna thickness L , and the cap thickness ΔL . The Gaussian baseline is located at $x_0 - L/2$, and the Gaussian amplitude was set so that the Gaussian fits the parabola with the same set of parameters [compare Fig. 2(d)].

In Fig. 6(a), we scan over the rear radius, $0.89 \mu\text{m} \leq r_{\min} \leq 1.75 \mu\text{m}$. For small r_{\min} , the maximum B-field strength rises linearly, before reaching an optimal value of 9.5 T at $r_{\min} = 1.5 \mu\text{m}$. For larger r_{\min} , the maximum B-field strength falls rapidly within few tens of nanometers, showing a different behavior than observed for the parabolic antenna. Figure 6(b) shows that for the Gaussian antenna, the enhanced B-field is broadly distributed and does not follow the focal point of the parabola fitting the Gaussian (red line). This can be rationalized as only the region close to the vertex resembles a concave parabolic shape but further away from the beam axis

changes to a convex shape that does not confine the B-field. Consistent with the low maximum B-field strength and the large spread of the B-field, Fig. 6(c) shows no needle-like or spot-like confinement of the B-field.

The antenna length scan of the Gaussian antenna is shown in Fig. 6(d). The rear radius r_{\min} was fixed to the value that maximized the B-field for the parabolic antenna. For thin Gaussian antennas ($L < 0.3 \mu\text{m}$) the B-field strength grows slowly, while at thicker antenna lengths ($0.3 \mu\text{m} \leq r_{\min} \leq 1.2 \mu\text{m}$) we observe a faster increase in B-field strength. The maximum B-field strength in this scan, 32 T, is reached at about $L = 1.45 \mu\text{m}$, which, surprisingly, exceeds the maximum B-field strength from the analogous scan in Fig. 5(d) (25 T at $L = 0.7 \mu\text{m}$). As depicted in Fig. 6(e), the maximum B-field spot is located in front of the hypothetical focal point, independent of L . This indicates that the Gaussian antenna with the chosen parameters does not behave like the fitted parabola. The snapshot of the most intense B-field [Fig. 6(f)] within all simulations of the performed scan reveals that the maximum B-field is built up inside the aperture.

In the cap thickness (ΔL) scan shown in Fig. 6(g), the same parameters were fixed and scanned, respectively, as in the analogous scan of the parabolic antenna. Remarkably, the maximum B-field is nearly constant over the scanned cap thickness, showing a value of about 30 T for nearly closed and fully closed antennas. This value is considerably smaller than the maximum B-field reached for the parabolic antenna—which reached up to 47 T [Fig. 5(g)]—but nonetheless shows a substantial enhancement of the B-field. In Fig. 6(h), we see that the maximum

B-field spot is located on the front side of the antenna, and that no B-field reaches the vertex of the Gaussian profile. Overall, the B-field enhancement in a Gaussian antenna is not as advantageous as in the parabolic antenna, where the constructive interference is more favorable, as evidenced in Fig. 6(i).

3. Logarithmic Antenna

Our final considered antenna geometry presents a logarithmic profile [see Fig. 2(e)]. In contrast to the Gaussian antenna profile, it exhibits a globally convexly curved profile. The front radius is fixed to $r_{\max} = 1.77 \mu\text{m}$ (as in all previous computations), which leaves two independent parameters (see Table 1), the decay parameter κ and the antenna length L .

In Fig. 7(a), the antenna decay parameter is scanned in the interval $0.12 \mu\text{m}^{-1} \leq \kappa \leq 12 \mu\text{m}^{-1}$. The antenna thickness was fixed at $L = 0.42 \mu\text{m}$. We observe a maximum B-field peak around $\kappa = 1.15 \mu\text{m}^{-1}$ with a B-field strength of 21 T. For smaller decay parameters, the maximum achievable B-field quickly drops off, until the logarithmic antenna resembles the cylindrical one at $\kappa = 0.0 \mu\text{m}^{-1}$. For κ values larger than the optimum, the rear antenna radius (r_{\min}) decreases (exponentially) until the antenna is nearly closed, leading to a strong reduction in the maximum achievable B-field that is even lower than for free beam propagation. As shown in Fig. 7(b), at small κ values the (open) antenna works similar to the other presented antennas with a maximum B-field spot whose position (rear to front) depends sensitively on κ . At larger κ values, the antenna is nearly closed and does not enhance the B-field. In the optimal case, for $\kappa = 1.15 \mu\text{m}^{-1}$, the maximum

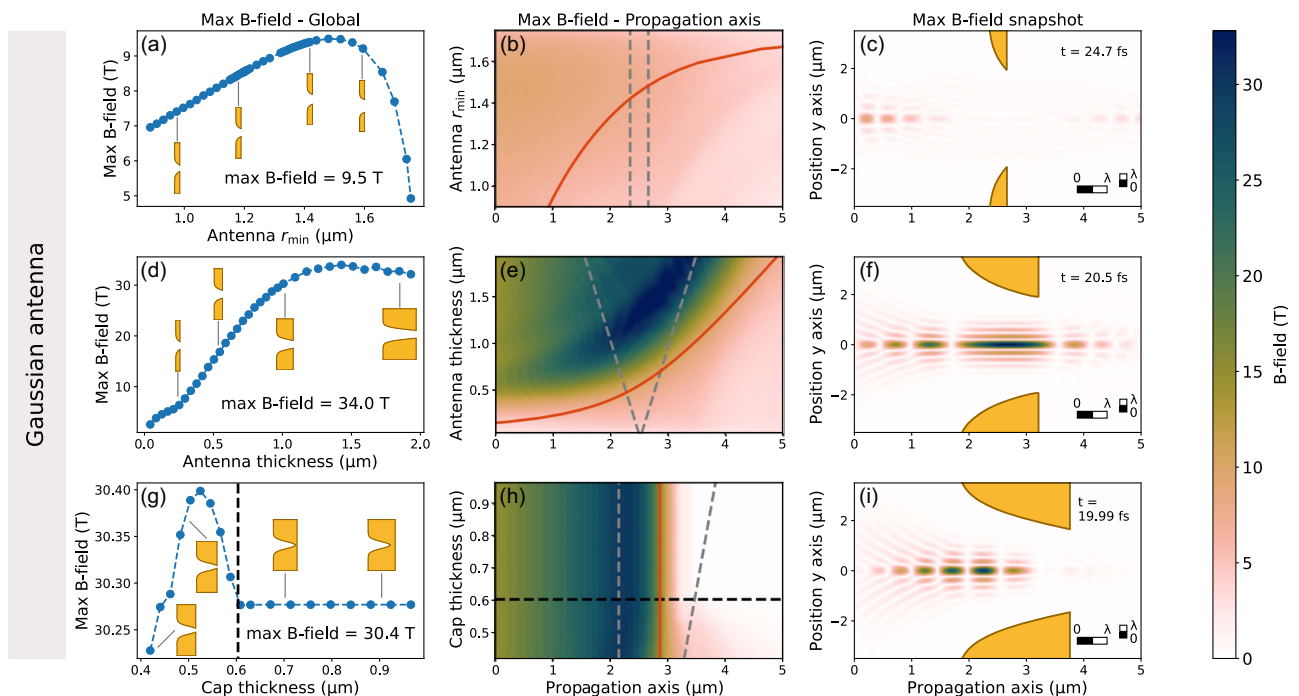


Fig. 6. Absolute B-field strength for the Gaussian antenna for scans of r_{\min} (a)–(c), antenna thickness L (d)–(f), and cap thickness ΔL (g)–(i). In the first column (a), (d), (g), the maximum B-field on the propagation axis is shown depending on the scanned parameter. The second column (b), (e), (h) shows the distribution of the B-field strength along the propagation axis, the longitudinal extent of the aperture (gray dashed lines), and the position of the focal point (red, solid line). In the third column (c), (f), (i), a temporal snapshot of the highest B-field strength is presented for the different scans. The dashed black line in (g) and (h) indicates when the antenna is closed.

B-field spot is located inside the antenna, close to the front edge. The maximum B-field spot position is more readily visible in the snapshot in Fig. 7(c).

In the antenna thickness scan shown in Fig. 7(d), the parameters $\kappa = 1.15 \mu\text{m}^{-1}$ and $r_{\text{max}} = 1.77 \mu\text{m}$ were kept fixed, and the thickness was varied in the interval $L = 0.04 \mu\text{m}$ to $L = 0.97 \mu\text{m}$. The maximum B-field strength grows approximately linearly between $L = 0.04 \mu\text{m}$ and about $L = 0.5 \mu\text{m}$, reaching its peak at $L = 0.68 \mu\text{m}$ with a B-field strength of about 25 T. For thicker antennas, the maximum B-field strength stays approximately constant. As shown in Fig. 7(e), the maximum B-field position is always in front of the antenna, only weakly depending on L . It can be observed that the B-field in the rear is always very weak, and thus we do not expect that a further increase in L would change the B-field distribution. The B-field snapshot shown in Fig. 7(f) is very similar to the one presented in Fig. 7(c), except for a slightly higher maximum B-field.

Overall, the logarithmic antenna can be compared most closely to the conical antenna. The results show that for similar parameters (r_{max} , effective r_{min} , L), the conical antenna provides a larger B-field enhancement. The maximum B-field achieved with the logarithmic antenna is about 22 T, whereas the conical antenna was able to deliver up to about 36 T (which is about 50% larger). This shows that already a small (convex) curvature of the antenna wall can substantially decrease the effectiveness of the device.

D. Magnetic-to-Electric Field Contrast

Up to now we have analyzed the B-field enhancement of an APB with a metallic nanoantenna. However, for applications not only the intensity of the B-field is important but also the spatial separation between the E-field and B-field components. For example, in an MD-only optical spectroscopy scheme, MD transitions can only be unambiguously distinguished from ED and electric quadrupole transitions if the E-field is effectively

suppressed [27,81]. To examine the isolation of the B-field from the E-field, we compute the intensity contrast, which we define as the c -scaled ratio of the square-integrated B-field and E-field, $c^2 \overline{B}^2 / \overline{E}^2$. The quantities \overline{B}^2 and \overline{E}^2 denote the temporally integrated B-field and E-field intensities, defined as

$$\overline{E}^2(\vec{r}) = \frac{1}{T} \int_0^T |E(\vec{r}, t)|^2 dt, \quad \overline{B}^2(\vec{r}) = \frac{1}{T} \int_0^T |B(\vec{r}, t)|^2 dt, \quad (4)$$

where T is the total simulation time.

In Fig. 8 we present the intensity contrast for the different aperture shapes considered in this work, using the optimal parameters mentioned above. First, we observe transverse regions of high contrast due to the interference between the incoming and reflected fields. Defining a desired contrast of 10 (for which the B-field intensity is one order of magnitude higher than the E-field intensity), these regions exhibit a thickness of about $x_c \approx 50 \text{ nm}$, about one tenth of the wavelength. Note that at the rear side of the antennas, the E-field and B-field are negligible, so the contrast is ill-defined. Otherwise, the different analyzed geometries show quite similar intensity contrast distributions, with only minor differences near the antenna edges.

Second and more relevant, all antennas exhibit diverging contrast near the propagation axis, as expected from the symmetry of the incident APB. The radial extension of this central region in which the contrast is larger than 10 is $\rho_c \approx 60 \text{ nm}$, whereas it remains larger than 1 up to $\rho'_c \approx 100 \text{ nm}$. The asymptotic behavior of the intensity contrast for small ρ can be derived from Eq. (1), for the incident beam, and Eq. (2) and assuming $\rho \ll w_0$:

$$\frac{c^2 \overline{B}^2}{\overline{E}^2} \sim 1 + \left(\frac{\lambda}{\pi \rho} \right)^2. \quad (5)$$

As expected, the intensity contrast exhibits a singularity at $\rho = 0$ and diverges as ρ^{-2} . All simulated antennas, being

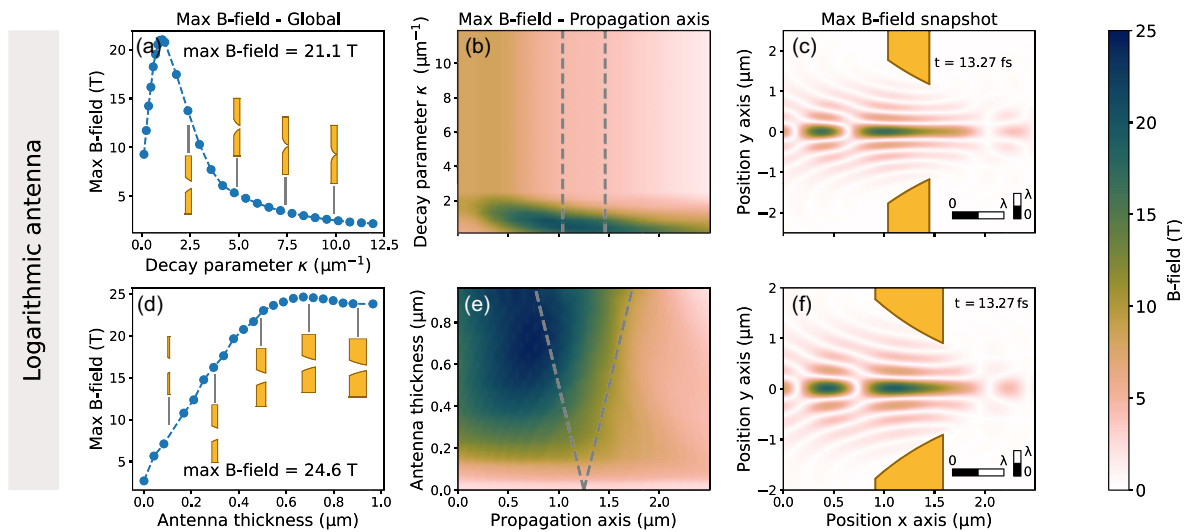


Fig. 7. Absolute B-field strength for the logarithmic antenna for (a)–(c) scans of κ and (d)–(f) antenna thickness L . (a), (d) In the first column, the maximum B-field on the propagation axis is shown depending on the scanned parameter. (b), (e) The second column shows the distribution of the B-field strength along the propagation axis and the longitudinal extent of the aperture (gray dashed lines). (c), (f) In the third column, a temporal snapshot of the highest B-field strength is presented for the different scans.

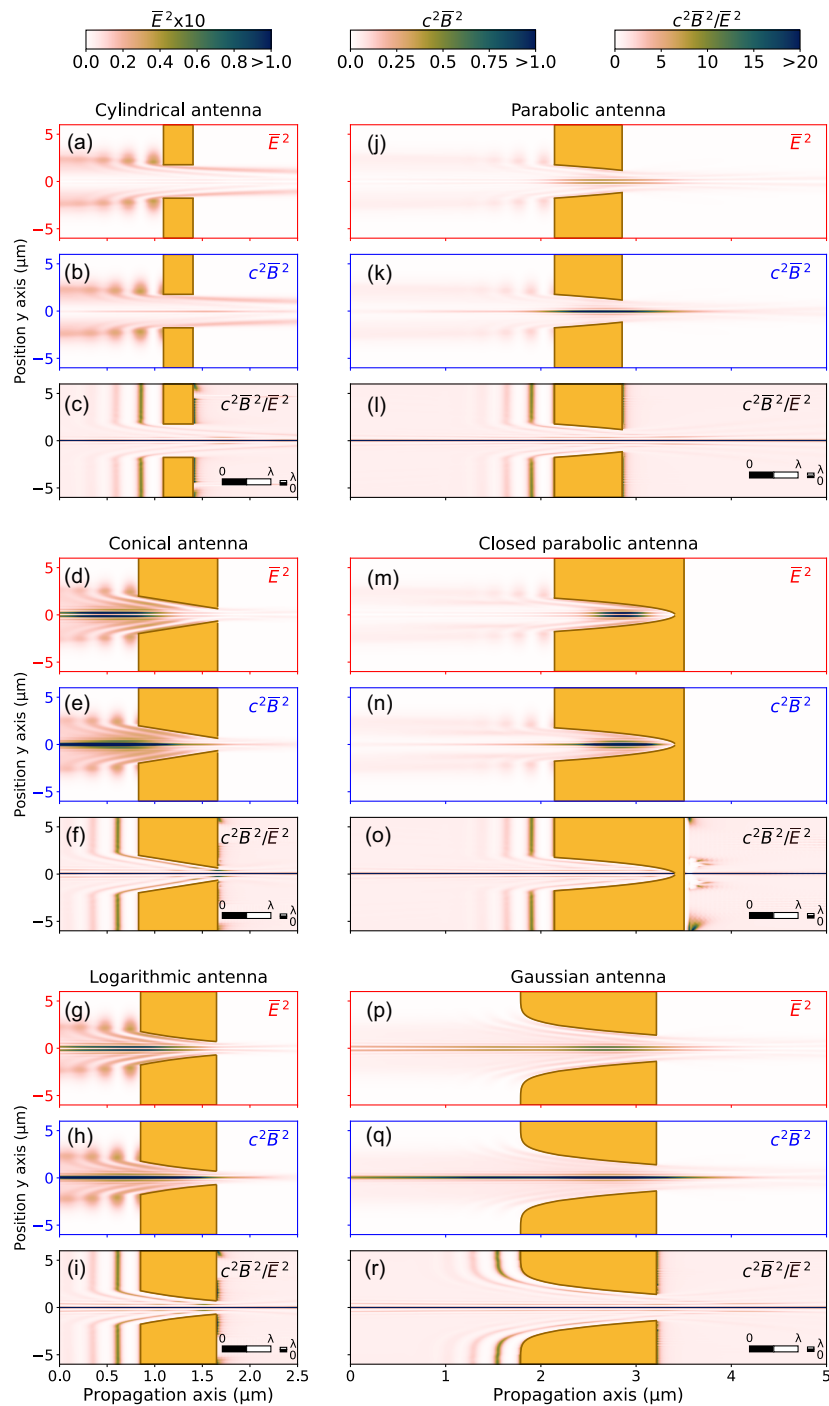


Fig. 8. Temporally integrated squared-integrated E-field/B-field (red/blue) and intensity contrast $\frac{c^2 \bar{B}^2}{\bar{E}^2}$ for the (a)–(c) cylindrical, (d)–(f) conical, (g)–(i) logarithmic, (j)–(l) parabolic, (m)–(o) closed parabolic, and (p)–(r) Gaussian antenna geometries. For each antenna, the optimal parameters (see above) were used.

cylindrically symmetric, exhibit such singularity in the intensity contrast. In order to see how the intensity contrast decreases along the radial coordinate for different antennas, we plot in Fig. 9 the intensity contrast near the beam axis for the optimized cases. Near the propagation axis ($\rho \approx 0$), the intensity contrast follows the analytical estimation for a free APB, given by Eq. (5) (black line). Away from the propagation axis, the antenna

geometry imprints subtle differences. Looking at Eq. (5), the most promising way to increase the volume of the high-contrast regions is by considering longer laser wavelengths, a potential scenario for the emerging mid- and far-infrared laser systems with applications not limited to spectroscopic studies but interesting for driving and controlling magnetic samples [23], or for photoinduced force microscopy [21].

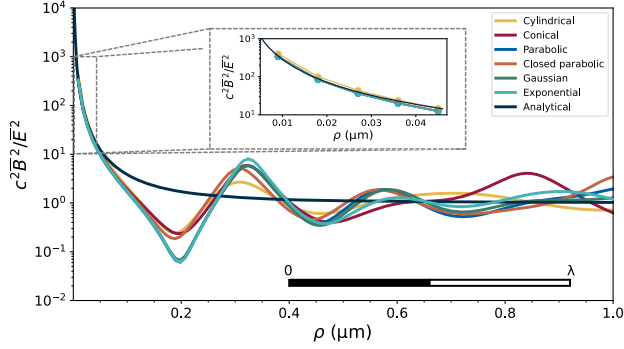


Fig. 9. Transverse distribution of the intensity contrast $\frac{c^2 B^2}{E^2}$ for different antenna geometries (see Fig. 8) at the transverse plane in the center of the simulation box. The abscissa shows only positive values for y (equivalent to ρ), as the simulation obeys cylindrical symmetry in the transverse direction.

4. CONCLUSION

Our study provides a wide perspective for the generation of intense and isolated B-fields from structured laser beams. We have demonstrated that the use of ultrafast APBs in tailored metallic nanoantennas provides intense longitudinal B-fields near the beam axis, highly isolated from the corresponding E-field. Our PIC numerical simulations show how the B-field carried by an APB can be highly amplified if using tailored antennas. For example, the use of conical antennas provides a gain factor up to ~ 50 over an extended spatial region, whereas closed parabolic antennas provide a highly confined B-field with a gain factor of ~ 65 . This setup allows obtaining isolated B-fields of up to ~ 50 T from moderately intense femtosecond APBs (peak intensity of 1.9×10^{11} W/cm²) at a central wavelength of 527.5 nm. It also opens a very promising route to perform MD-only optical spectroscopic studies with state-of-the-art laser technology. We emphasize that the simultaneous isolation and enhancement of the B-fields distinguish the presented setup from other B-field enhancement or B-field isolation schemes.

We have developed an analytical model that explains the mechanism behind the B-field enhancement in terms of phase-matching between induced current loops along the propagation axis. The model also allows characterizing the spatial extent of the B-field needle, which expands over hundreds of nm for the parameters considered. We have presented a systematic study using linearly sloped and curved sloped antennas, including cylindrical, conical, parabolic, Gaussian, and logarithmic shapes, showing their suitability to provide intense and highly isolated B-fields.

Finally, we have analyzed the intensity contrast, i.e., the magnetic-to-electric field ratio, that allows us to define the isolated B-field region. The radial extension where the B-field intensity is larger than the E-field intensity extends up to 100 nm, with similar results for all the explored antenna geometries. Note that the achieved outcomes are scalable beyond the specified central wavelength used in this work, $\lambda = 527.5$ nm, which was picked due to its relevance in MD-only absorption

spectroscopy experiments in Eu³⁺ ions. Far-infrared and terahertz sources (in combination with appropriately sized antennas) would allow the realization of larger isolated longitudinal B-field volumes, most suitable for a broad spectrum of technological applications ranging from magnetic spectroscopy to controlling ultrafast magnetization dynamics.

APPENDIX A: DEFINITION OF THE ANTENNA SHAPES

We explore the longitudinal B-field amplification from azimuthally polarized beams interacting with five different antenna geometries: cylindrical, conical, parabolic, Gaussian, and logarithmic. The mathematical expressions and the scanned parameters for each profile are formally given in Table 1. A visual sketch of the parameters in every antenna can be seen in Fig. 2. The metallic antennas are centered in the simulation box. Parameters x_{\min} and x_{\max} refer to the simulation box edges in the propagation axis.

APPENDIX B: ANALYTICAL MODEL

The APB will induce a set of fast oscillating current loops in the metallic antenna, and the total B-field will result from the superposition of the contributions from all these current loops. We start by determining the B-field created by a thin current loop and then integrating over all the loops contained in the antenna thickness.

The induced current distribution in the aperture can be expressed as

$$\vec{j}(\rho', \phi', x', t) = j_0(x') \delta(\rho' - \rho_0) \delta(x' - x_0) e^{i\frac{2\pi}{\lambda}(x' - ct)} \vec{u}_\phi, \quad (\text{B1})$$

where j_0 is the current density amplitude, ρ_0 is the aperture radius, and x_0 is the central longitudinal position of the

Table 1. Definitions of the Simulated Antenna Shapes by Analytical Expressions and Considered Scan Parameters, Assuming $x \in [x_0 - L/2, x_0 + L/2 + \Delta L]$

Antenna Shape	Formula	Scan Parameters
Cylindrical	$\rho(x) = r_0$	L
Conical	$c_c = \frac{x_{\max} - x_{\min} - L}{2}$ $\rho(x) = r_{\max} - \frac{r_{\max} - r_{\min}}{L} (x - c_c)$	r_{\min}, r_{\max}
Parabola	$f = \frac{r_{\max}^2 - r_{\min}^2}{4L}$ $c_p = \frac{r_{\max}^2}{4f}$ $\rho(x) = 2\sqrt{f \cdot (c_p - x)}$	$r_{\min}, L, \Delta L$
Gaussian	$\sigma = \frac{r_{\max}}{2}$ $c_G = \frac{x_{\max} - x_{\min} - L}{2}$ $A = \frac{r_{\max}^2}{4f}$ $\rho(x) = \sqrt{-2\sigma^2 \cdot \ln\left(\frac{x - c_G}{A}\right)}$	$r_{\min}, L, \Delta L$
Logarithmic	$c_e = \frac{x_{\max} - x_{\min} - L}{2}$ $\rho(x) = r_{\max} e^{-\kappa(x - c_e)}$	κ, L

aperture. Strictly, this plane wave solution is not applicable for the curved wavefronts of tightly focused laser beams; still, they may be utilized in this context as first approximation. The retarded vector potential associated to a current can be obtained, in cylindrical coordinates, as

$$\vec{A}(\vec{r}) = \frac{1}{c} \iiint d\rho' d\phi' dx' \rho' \frac{\vec{j}(\rho', \phi', x', t_{\text{ret}})}{|\vec{r} - \vec{r}'|} \hat{u}_\phi, \quad (\text{B2})$$

where we used the Coulomb gauge. The primed coordinates refer to the source points, and $t_{\text{ret}} = \frac{1}{c}(x' - |\vec{r} - \vec{r}'|)$, with $\vec{r} = (\rho, \phi, x)^T$, is the retarded time. In this way, we account for the temporal difference between the instant at which the laser beam, approximated by a plane wave, hits the respective aperture source point r' and the time that the generated (electro-)magnetic fields at r' take to arrive at the observer at position r . Using Eq. (B1) and the definition of retarded time in the previous expression we get

$$A_\phi(\vec{r}) = \frac{j_0(x_0)}{c} \rho_0 e^{i\frac{2\pi}{\lambda}(x_0 - ct)} \int d\phi' \cos(\phi') \times \frac{e^{i\frac{2\pi}{\lambda}(\rho^2 + \rho_0^2 - 2\rho\rho_0 \cos\phi' + (x - x_0)^2)^{1/2}}}{(\rho^2 + \rho_0^2 - 2\rho\rho_0 \cos(\phi') + (x - x_0)^2)^{1/2}}. \quad (\text{B3})$$

The corresponding B-field is obtained as $\vec{B} = \nabla \times \vec{A}$. The longitudinal component of the B-field, close to the optical axis, can be approximated as

$$B_{x,0}(x) = \lim_{\rho \rightarrow 0} (\nabla \times \vec{A})_x = 2 \left(\frac{\partial A_\phi(\vec{r})}{\partial \rho} \right)_{\rho=0}, \quad (\text{B4})$$

resulting in the following expression for the approximate longitudinal B-field created by a thin loop in the optical axis:

$$B_{x,0}(x) = 2\pi \frac{j_0(x_0)}{c} \frac{\rho_0^2}{\rho_0^2 + (x - x_0)^2} \left(\left(\frac{2\pi}{\lambda} \right)^2 + \frac{1}{\rho_0^2 + (x - x_0)^2} \right)^{1/2} \times e^{i\frac{2\pi}{\lambda}(x_0 + \sqrt{\rho_0^2 + (x - x_0)^2} - ct) - i \arctan\left(\frac{2\pi}{\lambda} \sqrt{\rho_0^2 + (x - x_0)^2}\right)}. \quad (\text{B5})$$

To obtain the whole longitudinal B-field created by a thick antenna, we integrate Eq. (B5), which is valid for a single current loop, over the antenna thickness. Thus, it is necessary to include the dependency of the aperture radius $\rho_0 \Rightarrow \rho_0(x')$, as well as the current density $j_0(x_0) \Rightarrow j_0(x')$ on the source position,

$$B_x(x) = 2\pi \int dx' \frac{j_0(x')}{c} \frac{\rho_0(x')^2}{\rho_0(x')^2 + (x - x')^2} \times \left(\left(\frac{2\pi}{\lambda} \right)^2 + \frac{1}{\rho_0(x')^2 + (x - x')^2} \right)^{1/2} \times e^{i\frac{2\pi}{\lambda}(x' + \sqrt{\rho_0(x')^2 + (x - x')^2} - ct) - i \arctan\left(\frac{2\pi}{\lambda} \sqrt{\rho_0(x')^2 + (x - x')^2}\right)}. \quad (\text{B6})$$

The first factor inside the integral denotes the current density distribution $j_0(x')$. It is related to the electrons density and velocity by $j_0(x') = qnv(x')$, where q is the electron's charge, n is the density, and $v(x')$ is the velocity. The electron's mean velocity can be calculated classically equaling the laser ponderomotive energy $U_p = q^2 E_0^2 / 4m_e \omega^2$ to the electron's kinetic energy,

$$v(x') = \frac{qE_0(x')}{\sqrt{2}m_e\omega} \Gamma(x'), \quad (\text{B7})$$

where the longitudinal change of aperture radius along the x' coordinate is implemented in the E-field amplitude E_0 . The $\Gamma(x')$ factor takes into account the effect of the antenna curvature and is defined as

$$\Gamma(x') = 1 - \cos\left(\arctan\left(\frac{\partial}{\partial x'} \rho(x')\right)\right). \quad (\text{B8})$$

The second and third factors in Eq. (B6) describe the decrease in B-field if the observer point x is shifted away from the current loop position x' . The phase factor is discussed in Section 3.B.

Funding. European Research Council (851201); Ministerio de Ciencia e Innovación (PID2022-142340NB-I00, PID2019-106910GB-I00); Austrian Science Fund (10.55776/ZK91).

Acknowledgment. L. G. and S. M. also thank Valentina Shumakova, Elizaveta Gangrskaja, Alessandra Bellissimo, Audrius Pugzlys, and Andrius Baltuška for fruitful discussions and computational support by the Vienna Scientific Cluster (VSC 4). The authors thankfully acknowledge the computer resources at MareNostrum and SCAYLE, and the technical support provided by Barcelona Supercomputing Center (RES-FI-2022-3-0041).

R. M.-H., L. S.-T., L. P., E. C. J., and C. H.-G. acknowledge funding from the European Research Council (ERC) under the European Union's Horizon 2020 research and innovation program (Grant Agreement No. 851201) and support from Ministerio de Ciencia e Innovación (PID2022-142340NB-I00, PID2019-106910GB-I00). This research was funded in whole or in part by the Austrian Science Fund (FWF) (10.55776/ZK91). For open access purposes, the author has applied a CC BY public copyright license to any author accepted manuscript version arising from this submission.

Disclosures. The authors declare no conflicts of interest.

Data Availability. Data underlying the results presented in this paper are not publicly available at this time but may be obtained from the authors upon reasonable request.

REFERENCES

1. A. Forbes, "Structured light from lasers," *Laser Photon. Rev.* **13**, 1900140 (2019).
2. C. He, Y. Shen, and A. Forbes, "Towards higher-dimensional structured light," *Light Sci. Appl.* **11**, 205 (2022).
3. K. Y. Bliokh, E. Karimi, M. J. Padgett, *et al.*, "Roadmap on structured waves," *J. Opt.* **25**, 103001 (2023).
4. S. Karaveli and R. Zia, "Spectral tuning by selective enhancement of electric and magnetic dipole emission," *Phys. Rev. Lett.* **106**, 193004 (2011).
5. F. T. Rabouw, P. T. Prins, and D. J. Norris, "Europium-doped NaYF₄ nanocrystals as probes for the electric and magnetic local density of optical states throughout the visible spectral range," *Nano Lett.* **16**, 7254–7260 (2016).

6. B. Reynier, E. Charron, O. Markovic, *et al.*, "Full control of electric and magnetic light-matter interactions through a nanomirror on a near-field tip," *Optica* **10**, 841–845 (2023).
7. M. Sanz-Paz, C. Ermandes, J. U. Esparza, *et al.*, "Enhancing magnetic light emission with all-dielectric optical nanoantennas," *Nano Lett.* **18**, 3481–3487 (2018).
8. R. Hussain, S. S. Kruk, C. E. Bonner, *et al.*, "Enhancing Eu³⁺ magnetic dipole emission by resonant plasmonic nanostructures," *Opt. Lett.* **40**, 1659–1662 (2015).
9. M. Montagnac, Y. Brûlé, A. Cuche, *et al.*, "Control of light emission of quantum emitters coupled to silicon nanoantenna using cylindrical vector beams," *Light Sci. Appl.* **12**, 239 (2023).
10. E. M. Purcell, H. C. Torrey, and R. V. Pound, "Resonance absorption by nuclear magnetic moments in a solid," *Phys. Rev.* **69**, 37–38 (1946).
11. M. Veysi, C. Guclu, and F. Capolino, "Vortex beams with strong longitudinally polarized magnetic field and their generation by using metasurfaces," *J. Opt. Soc. Am. B* **32**, 345–354 (2015).
12. A. Bashiri, A. Vaskin, K. Tanaka, *et al.*, "Color routing of the emission from magnetic and electric dipole transitions of Eu³⁺ by broken-symmetry TiO₂ metasurfaces," *ACS Nano* **18**, 506–514 (2024).
13. R. Martín-Hernández, H. Hu, A. Baltuska, *et al.*, "Fourier-limited attosecond pulse from high harmonic generation assisted by ultrafast magnetic fields," *Ultrafast Sci.* **3**, 0036 (2023).
14. M. Chekhova and P. Banzer, *Polarization of Light: In Classical, Quantum, and Nonlinear Optics* (De Gruyter, 2021).
15. Q. Zhan, "Cylindrical vector beams: from mathematical concepts to applications," *Adv. Opt. Photon.* **1**, 1–57 (2009).
16. H. Rubinsztein-Dunlop, A. Forbes, M. V. Berry, *et al.*, "Roadmap on structured light," *J. Opt.* **19**, 013001 (2017).
17. Y. Shen, Q. Zhan, L. G. Wright, *et al.*, "Roadmap on spatiotemporal light fields," *J. Opt.* **25**, 093001 (2023).
18. M. Veysi, C. Guclu, and F. Capolino, "Focused azimuthally polarized vector beam and spatial magnetic resolution below the diffraction limit," *J. Opt. Soc. Am. B* **33**, 2265–2277 (2016).
19. J. R. Zurita-Sánchez and L. Novotny, "Multipolar interband absorption in a semiconductor quantum. II. Magnetic dipole enhancement," *J. Opt. Soc. Am. B* **19**, 2722–2726 (2002).
20. P. Woźniak and P. Banzer, "Single nanoparticle real and *k*-space spectroscopy with structured light," *New J. Phys.* **23**, 103013 (2021).
21. J. Zeng, F. Huang, C. Guclu, *et al.*, "Sharply focused azimuthally polarized beams with magnetic dominance: near-field characterization at nanoscale by photoinduced force microscopy," *ACS Photon.* **5**, 390–397 (2018).
22. I. Rajapaksa, K. Uenal, and H. K. Wickramasinghe, "Image force microscopy of molecular resonance: a microscope principle," *Appl. Phys. Lett.* **97**, 073121 (2010).
23. L. Sánchez-Tejerina, R. Martín-Hernández, R. Yanes, *et al.*, "All-optical non-linear chiral ultrafast magnetization dynamics driven by circularly polarized magnetic fields," *High Power Laser Sci. Eng.* **11**, e82 (2023).
24. M. Burreli, D. Van Oosten, T. Kampfrath, *et al.*, "Probing the magnetic field of light at optical frequencies," *Science* **326**, 550–553 (2009).
25. T. H. Taminiau, S. Karaveli, N. F. van Hulst, *et al.*, "Quantifying the magnetic nature of light emission," *Nat. Commun.* **3**, 979 (2012).
26. S. Bernadotte, A. J. Atkins, and C. R. Jacob, "Origin-independent calculation of quadrupole intensities in X-ray spectroscopy," *J. Chem. Phys.* **137**, 204106 (2012).
27. M. Kasperczyk, S. Person, D. Ananias, *et al.*, "Excitation of magnetic dipole transitions at optical frequencies," *Phys. Rev. Lett.* **114**, 163903 (2015).
28. C. J. Foot, *Atomic Physics*, Oxford Master Series in Atomic, Optical and Laser Physics (Oxford University, 2005), Vol. 7.
29. O. Laporte and W. F. Meggers, "Some rules of spectral structure," *J. Opt. Soc. Am.* **11**, 459–463 (1925).
30. W. W. Parson, *Modern Optical Spectroscopy* (Springer, 2015).
31. D. J. Clouthier and D. A. Ramsay, "The spectroscopy of formaldehyde and thioformaldehyde," *Annu. Rev. Phys. Chem.* **34**, 31–58 (1983).
32. M. Klessinger and J. Michl, *Excited States and Photochemistry of Organic Molecules* (VCH, 1995).
33. J. R. Platt, "Classification of spectra of cata-condensed hydrocarbons," *J. Chem. Phys.* **17**, 484–495 (1949).
34. R. R. Valiev, G. V. Baryshnikov, and D. Sundholm, "Relations between the aromaticity and magnetic dipole transitions in the electronic spectra of hetero[8]circulenes," *Phys. Chem. Chem. Phys.* **20**, 30239–30246 (2018).
35. W. Mason, "Magnetic circular dichroism," in *Comprehensive Coordination Chemistry II* (Elsevier, 2003), pp. 327–337.
36. S. Rassou, A. Bourdier, and M. Drouin, "Influence of a strong longitudinal magnetic field on laser wakefield acceleration," *Phys. Plasmas* **22**, 073104 (2015).
37. P. Korneev, V. Tikhonchuk, and E. d'Humières, "Magnetization of laser-produced plasma in a chiral hollow target," *New J. Phys.* **19**, 033023 (2017).
38. J. Vieira, S. F. Martins, V. B. Pathak, *et al.*, "Magnetic control of particle injection in plasma based accelerators," *Phys. Rev. Lett.* **106**, 225001 (2011).
39. F. Huang, V. Ananth Tamma, Z. Mardy, *et al.*, "Imaging nanoscale electromagnetic near-field distributions using optical forces," *Sci. Rep.* **5**, 10610 (2015).
40. B. Hecht, B. Sick, U. P. Wild, *et al.*, "Scanning near-field optical microscopy with aperture probes: fundamentals and applications," *J. Chem. Phys.* **112**, 7761–7774 (2000).
41. F. Zenhausern, Y. Martin, and H. K. Wickramasinghe, "Scanning interferometric apertureless microscopy: optical imaging at 10 angstrom resolution," *Science* **269**, 1083–1085 (1995).
42. M. R. Beversluis, L. Novotny, and S. J. Stranick, "Programmable vector point-spread function engineering," *Opt. Express* **14**, 2650–2656 (2006).
43. V. G. Shvedov, C. Hnatovsky, N. Shostka, *et al.*, "Generation of vector bottle beams with a uniaxial crystal," *J. Opt. Soc. Am. B* **30**, 1–6 (2013).
44. A. Turpin, Yu. V. Loiko, A. Peinado, *et al.*, "Polarization tailored novel vector beams based on conical refraction," *Opt. Express* **23**, 5704–5715 (2015).
45. T. Hirayama, Y. Kozawa, T. Nakamura, *et al.*, "Generation of a cylindrically symmetric, polarized laser beam with narrow linewidth and fine tunability," *Opt. Express* **14**, 12839–12845 (2006).
46. M. Beresna, M. Gecevičius, and P. G. Kazansky, "Polarization sensitive elements fabricated by femtosecond laser nanostructuring of glass [invited]," *Opt. Mater. Express* **1**, 783–795 (2011).
47. B. Alonso, I. Lopez-Quintas, W. Holgado, *et al.*, "Complete spatiotemporal and polarization characterization of ultrafast vector beams," *Commun. Phys.* **3**, 151 (2020).
48. C. Hernández-García, A. Turpin, J. San Román, *et al.*, "Extreme ultraviolet vector beams driven by infrared lasers," *Optica* **4**, 520–526 (2017).
49. M. Blanco, F. Cambroner, M. T. Flores-Arias, *et al.*, "Ultraintense femtosecond magnetic nanoprobe induced by azimuthally polarized laser beams," *ACS Photon.* **6**, 38–42 (2019).
50. S. Sederberg, F. Kong, and P. B. Corkum, "Tesla-scale terahertz magnetic impulses," *Phys. Rev. X* **10**, 011063 (2020).
51. Y. Yang, H. T. Dai, and X. W. Sun, "Split ring aperture for optical magnetic field enhancement by radially polarized beam," *Opt. Express* **21**, 6845–6850 (2013).
52. T. Grosjean, M. Mivelle, F. I. Baida, *et al.*, "Diabolo nanoantenna for enhancing and confining the magnetic optical field," *Nano Lett.* **11**, 1009–1013 (2011).
53. M. Pancaldi, P. Vavassori, and S. Bonetti, "Terahertz metamaterials for light-driven magnetism," *arXiv*, arXiv:2311.07252 (2023).
54. R. A. Fonseca, L. O. Silva, F. S. Tsung, *et al.*, "OSIRIS: a three-dimensional, fully relativistic particle in cell code for modeling plasma based accelerators," in *International Conference on Computational Science* (2002), pp. 342–351.
55. R. A. Fonseca, S. F. Martins, L. O. Silva, *et al.*, "One-to-one direct modeling of experiments and astrophysical scenarios: pushing the envelope on kinetic plasma simulations," *Plasma Phys. Controlled Fusion* **50**, 124034 (2008).

56. R. A. Fonseca, J. Vieira, F. Fiuza, *et al.*, "Exploiting multi-scale parallelism for large scale numerical modelling of laser wakefield accelerators," *Plasma Phys. Controlled Fusion* **55**, 124011 (2013).
57. D. J. Griffiths, *Introduction to Electrodynamics* (Cambridge University, 2017).
58. J. D. Jackson, *Classical Electrodynamics*, 3rd ed. (Wiley, 1999).
59. B. Bihari, H. Eilers, and B. M. Tissue, "Spectra and dynamics of monoclinic Eu_2O_3 and $\text{Eu}^{3+}:\text{Y}_2\text{O}_3$ nanocrystals," *J. Lumin.* **75**, 1–10 (1997).
60. K. Binnemans, "Interpretation of europium(III) spectra," *Coord. Chem. Rev.* **295**, 1–45 (2015).
61. J. M. Dawson, "Particle simulation of plasmas," *Rev. Mod. Phys.* **55**, 403–447 (1983).
62. C. K. Birdsall and A. B. Langdon, *Plasma Physics via Computer Simulation*, Series in Plasma Physics (Taylor & Francis, 2004).
63. J. Derouillat, A. Beck, F. Pérez, *et al.*, "SMILEI: a collaborative, open-source, multi-purpose particle-in-cell code for plasma simulation," *Comput. Phys. Commun.* **222**, 351–373 (2018).
64. J. Siegel, O. Lyutakov, V. Rybka, *et al.*, "Properties of gold nanostructures sputtered on glass," *Nanoscale Res. Lett.* **6**, 96 (2011).
65. D. Gall, "Electron mean free path in elemental metals," *J. Appl. Phys.* **119**, 085101 (2016).
66. J. Krüger, D. Dufft, R. Koter, *et al.*, "Femtosecond laser-induced damage of gold films," *Appl. Surf. Sci.* **253**, 7815–7819 (2007).
67. A. N. Koya, M. Romanelli, J. Kuttruff, *et al.*, "Advances in ultrafast plasmonics," *Appl. Phys. Rev.* **10**, 021318 (2023).
68. K. Yee, "Numerical solution of initial boundary value problems involving Maxwell's equations in isotropic media," *IEEE Trans. Antennas Propag.* **14**, 302–307 (1966).
69. J.-L. Vay, "A new absorbing layer boundary condition for the wave equation," *J. Comput. Phys.* **165**, 511–521 (2000).
70. L. Grünewald, R. Martín-Hernández, L. Sánchez-Tejerina San José, *et al.*, "SI tailored metallic nanoantennas," *Zenodo*, <http://doi.org/10.5281/zenodo.10082669> (2023).
71. J. Cunha, T.-L. Guo, G. Della Valle, *et al.*, "Controlling light, heat, and vibrations in plasmonics and phononics," *Adv. Opt. Mater.* **8**, 2001225 (2020).
72. M. Kim, N. Park, H. J. Lee, *et al.*, "The latest trends in nanophotonics," *Nanophotonics* **11**, 2389–2392 (2022).
73. S. Kurtz and T. Perry, "A powder technique for the evaluation of nonlinear optical materials," *J. Appl. Phys.* **39**, 3798–3813 (1968).
74. H. Kollmann, X. Piao, M. Esmann, *et al.*, "Toward plasmonics with nanometer precision: nonlinear optics of helium-ion milled gold nanoantennas," *Nano Lett.* **14**, 4778–4784 (2014).
75. D. T. Schoen, T. Coenen, F. J. García De Abajo, *et al.*, "The planar parabolic optical antenna," *Nano Lett.* **13**, 188–193 (2013).
76. P. Li, S. Chen, H. Dai, *et al.*, "Recent advances in focused ion beam nanofabrication for nanostructures and devices: fundamentals and applications," *Nanoscale* **13**, 1529–1565 (2021).
77. H. Penketh, J. Bertolotti, and W. L. Barnes, "Optimal position of an emitter in a wavelength-scale parabolic reflector," *Appl. Opt.* **58**, 7957–7961 (2019).
78. M. I. Stockman, "Nanoplasmonics: past, present, and glimpse into future," *Opt. Express* **19**, 22029 (2011).
79. N. Vladov, J. Segal, and S. Ratchev, "Apparent beam size definition of focused ion beams based on scanning electron microscopy images of nanodots," *J. Vac. Sci. Technol. B* **33**, 041803 (2015).
80. A. C. Madison, J. S. Villarrubia, K.-T. Liao, *et al.*, "Unmasking the resolution-throughput tradespace of focused-ion-beam machining," *Adv. Funct. Mater.* **32**, 2111840 (2022).
81. C. Cohen-Tannoudji, B. Diu, and F. Laloë, *Quantenmechanik. Band 2*, 5th ed. (De Gruyter, 2019).